

Article

Suspended Sediment Concentration and Fluxes in the High-Turbidity Zone in the Macro-Tidal Hangzhou Bay

Xin Chen ¹, Hui Shen ² , Jinxiong Yuan ³ and Li Li ^{1,*} 

¹ Institute of Port, Coastal and Offshore Engineering, Ocean College, Zhejiang University, Zhoushan 316021, China; 22134183@zju.edu.cn

² Marine Monitoring and Forecasting Center of Zhejiang Province, Hangzhou 310007, China

³ Hangzhou Xi'ao Environmental Sci-Tech Co., Ltd., Hangzhou 310000, China

* Correspondence: lilizju@zju.edu.cn; Tel.: +86-151-6841-1398

Abstract: The turbidity maximum zone (TMZ) plays an important role in the morphology and ecosystems of estuaries. The distributions of TMZ in Hangzhou Bay (HZB) and mechanisms of sediment fluxes in TMZ have been studied by applying a fully calibrated three-dimensional baroclinic model that considers salinity, high turbidity, sediment flocculation, and density coupling between water and sediment. Based on the method of SSC thresholds, the TMZ is mainly distributed from YG (Yanguan, toponymy in HZB) to ZP (Zhapu, toponymy in HZB). S1 and S2 are the cross-sections within the TMZ. Along the estuary, there is an ascending-to-descending trend observed in the monthly averaged bed current shear stress, while the monthly averaged density displays a descending-to-ascending pattern. The orientation of the monthly averaged surface fluxes of suspended sediment within the TMZ shows a clockwise circular pattern. Moreover, the net flux of suspended sediment along the estuary at section S1 is seaward, while at the section S2, it is landward. The high bottom stress and the sediment fluxes facilitate the retention, deposition, and enrichment of sediment within the TMZ. The suspended sediment fluxes at the two cross-sections was primarily influenced by Eulerian transport, Stokes transport, and tidal pumping transport. At cross-section S1, the sediment transport is dominated by tidal pumping. At cross-section S2, advective transport controls the sediment transportation near the deep northern bank; while near the southern bank of cross-section S2, tidal pumping is still the dominant factor. The outcome of this study provides a foundation for TMZ research in similar macro-tidal turbid estuaries around the world.

Keywords: TMZ; macro-tides; SSC; suspended sediment fluxes; formation mechanism



Citation: Chen, X.; Shen, H.; Yuan, J.; Li, L. Suspended Sediment Concentration and Fluxes in the High-Turbidity Zone in the Macro-Tidal Hangzhou Bay. *J. Mar. Sci. Eng.* **2023**, *11*, 2004. <https://doi.org/10.3390/jmse11102004>

Academic Editor: George Kontakiotis

Received: 19 September 2023

Revised: 6 October 2023

Accepted: 13 October 2023

Published: 18 October 2023



Copyright: © 2023 by the authors. Licensee MDPI, Basel, Switzerland. This article is an open access article distributed under the terms and conditions of the Creative Commons Attribution (CC BY) license (<https://creativecommons.org/licenses/by/4.0/>).

1. Introduction

The turbidity maximum zone (TMZ) is a turbid water body in which the sediment content is stably higher than that upstream and downstream and shows regular migration within a certain range in the estuary [1–3]. It was firstly discovered and defined by the French scholar Glangeaud in the Gironde Estuary, as cited in Burchard [4]. As an endemic phenomenon during the water and sediment transportation process in estuaries [5], the TMZ is crucial in shaping the estuarine morphology, shoals, and river mouth bars [6–9]. Hence, it significantly impacts the planning and layout of estuarine areas, such as the construction of harbors and navigational channels, the fishery farming, and tourism [10–12].

Researchers have carried out numerous studies on the TMZ in estuaries worldwide, e.g., the Chesapeake Bay in USA [13], the Tamar Estuary in UK [14], the Gironde Estuary in France [15], the Chikugo River estuary in Japan [16], the Brisbane River estuary in Australia [17], the Sabaki Estuary in Kenya [18], and the Changjiang estuary in China [10]. Much interest has been paid to the mechanisms of TMZ in different types of estuaries. These mechanisms mainly include estuarine circulation [19,20], tidal action [21,22], sediment settling and starting hysteresis effects [23,24], salt and freshwater mixing [12,25],

flocculation of suspended sediment [26,27], and sediment resuspension [28,29]. Estuarine circulation and tidal action are important macroscopic hydrodynamic processes that play a significant part in the formation and growth of TMZ in different estuaries. Other factors contributing to the development of TMZ are more localized and microscopic in nature. These factors primarily involve enhancing sediment retention, promoting aggregation trends, and maintaining suspension, reflecting the unique environmental characteristics of each estuary [3,25].

In-depth analyses of the formation mechanism and changing patterns of TMZ have revealed that the development of TMZ in various types of estuaries is influenced by different dominant dynamic processes and major controlling factors [3,25]. In general, weakly mixed estuaries are primarily driven by the estuarine circulation in the development of TMZ. In well-mixed estuaries, tides play the most important role. Partially mixed estuaries lie in between, where both the estuarine circulation and tides are indispensable in shaping the TMZ. The interaction among these drivers varies among estuary types, contributing to the diversity of TMZ development in different regions [3].

In weakly mixed and well-mixed estuaries, the tidal energy undergoes various processes during the landward propagation of the tidal wave from the outer seas. These processes include passing through the convergence of the estuaries, riverbed friction, and river–ocean interactions (e.g., backwater effect) [3,30]. As a consequence, the flow velocity and shear stress induced by the current both experience an initial increase and then a subsequent decrease along the estuaries [31]. As the ebb tides accelerate from upstream to the estuarine mouth and then disperse into the sea, the current-induced shear stress and the flow velocity rapidly decrease [25]. The sedimentation and suspension of bed sediment are mainly influenced by this shear stress. Consequently, the sediment is distributed regularly within the estuarine, with the highest sediment concentration typically occurring near the mouth, leading to the formation of the TMZ. Additionally, the tidal asymmetry causes a net sediment transport toward the land, which is concentrated in the dynamic equilibrium zone [3]. The dynamic equilibrium zone refers to the region where the integrals of shear stresses induced by the ebb and flood tidal currents are balanced [32]. This zone experiences dominance from the flood and ebb tides and oscillates accordingly, contributing significantly to the development of the TMZ [33,34]. It should also be noted that the study of the TMZ is still in its development. There are different understandings of their formation and evolution, influencing factors and mechanisms, which have not yet been unified [3].

Hangzhou Bay (HZB, Figure 1) broadly refers to the region where the Qiantang River discharges into the East China Sea. It is a representative example of macrotidal funnel-type estuary and is known for its highly turbid waters. The bay mouth spans about 100 km in width and gradually narrows to approximately 8 km at the bay head. The typical water depth at HZB is in the range of 8 to 10 m. HZB encompasses extensive muddy tidal flats along its southern coast. Notably, it is recognized as its powerful tidal bore, reaching heights of 9 m, which contributes to the high turbidity of its water. According to the field observation data, the suspended sediment concentration (SSC) in HZB could surpass 5 kg/m^3 at the surface layer [35]. Under the influence of runoff and topography, a significant amount of sediment is transported by powerful tides from the Changjiang River into the sea. This sediment accumulates from WJY (Wenjiayan) to ZP (Zhapu), creating a huge sand bar (Table A1). This sand bar stretches up to 130 km in length [36].

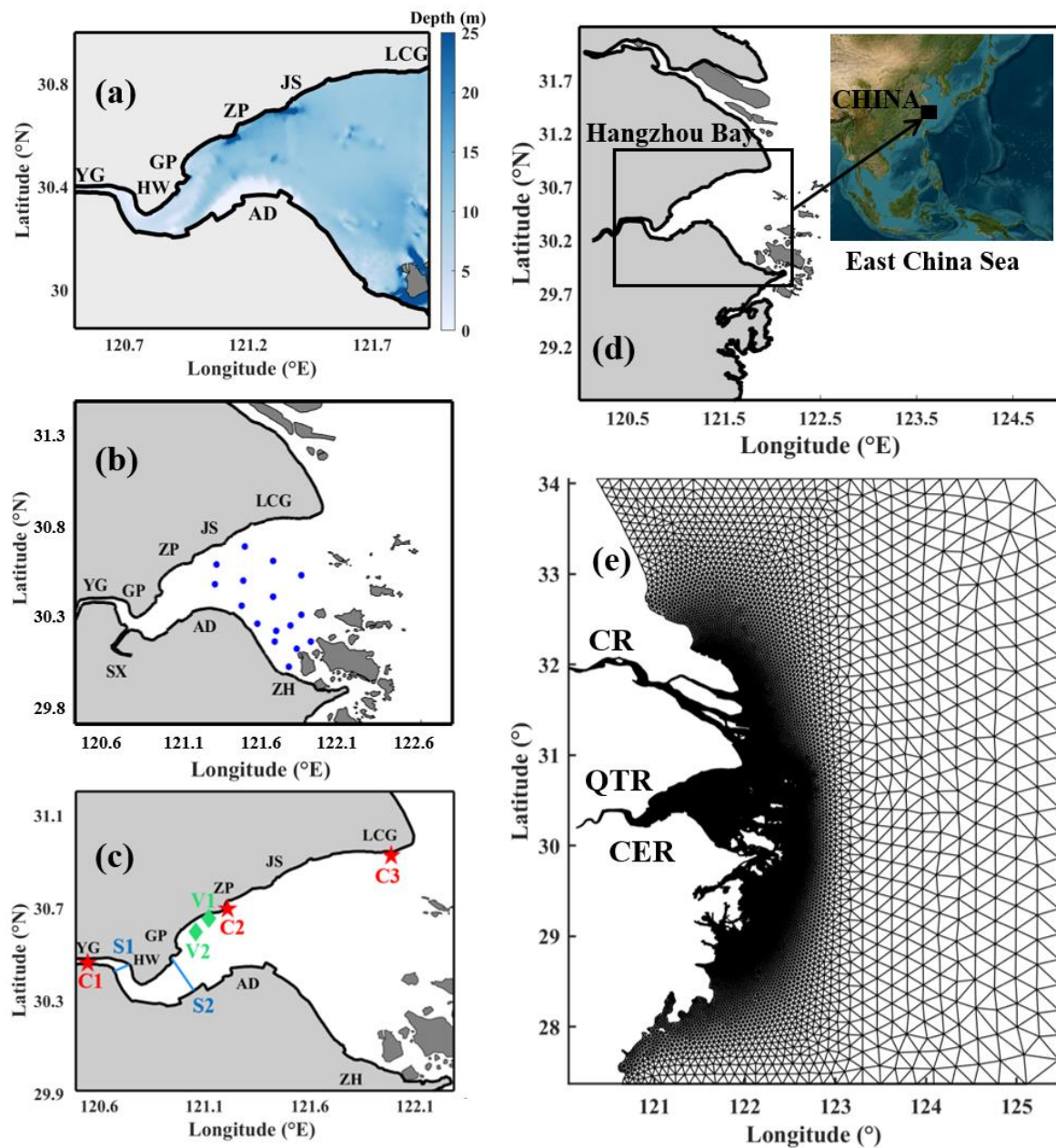


Figure 1. (a) Bathymetry in HZB. (b) Salinity field stations, locations of salinity are from Wang et al. [37]. (c) Field stations and two specific cross-sections. (d) The location of HZB. (e) Grids of the model domain. ZH: Zhenhai; HW: Huangwan (Jianshan); SX: Shaoxing; YG: Yanguan; JS: Jianshan; AD: Andong; LCG: Luchaogang. S1 and S2 denote the cross-sections, C1 to C3 the tidal height stations, V1 and V2 the SSC and tidal current stations. CR: the Changjiang River; QTR: the Qiantangjiang River; CER: the Cao'e'jiang River.

HZB has two prominent areas with high SSC: the GP (Ganpu) region and the region near the southern coast; along with a low SSC area between the bay's mouth and ZP on the northern coast [38]. The SSC is higher during winter and lower during summer. The island effect is associated with high values of SSC in HZB [39]. The sediment in HZB is predominantly composed of muddy chalk and silt, with coarser materials more prominent near the northern and southern shores, while finer materials are concentrated in the central region. The D_{50} (median particle size) of fine and coarse material are approximately 8 to 9 mm and 3 to 4 mm, respectively. The particle size transitions gradually from fine to coarse from the bay's mouth to its inner part [40].

According to the research conducted by Sun, the formation of the TMZ in strongly mixed estuaries in China could be attributed to several key factors [32]. One of the main reasons was the current-induced shear stress pattern, which exhibited an increase and then a decrease. This pattern, combined with the oppositely net sediment transport arising from the asymmetry of the tidal wave in the upstream and downstream estuary, led to the aggregation of sediment in the TMZ. Flocculation and sedimentation processes further enhanced the tendency of sediment retention and enrichment within the TMZ. These mechanisms worked together to create and maintain the TMZ in strongly mixed estuaries in China.

Previous studies have investigated the hydro-sediment characteristics of HZB using in situ measurements [41,42], modeling methods [43–46], and remote sensing [47,48]. However, less focus has been placed on understanding spatial distributions of the TMZ and the features and mechanisms of sediment transport within it. This study builds and fully validates a three-dimensional numerical model based on the FVCOM (Finite Volume Coastal Ocean Model). Given the high turbidity of HZB, the model incorporates the impact of SSC on water density, and the flocculation of fine sediment is also considered. The spatial distribution and possible formation mechanisms of TMZ are illustrated using model results. The numerical model was described in Section 2. Section 3 provides spatial and temporal variations in high SSC water bodies. The possible formation causes of TMZ are analyzed in Section 4. Section 5 presents the conclusion of the article.

2. Materials and Methods

2.1. Hydro-Sediment Model

Model descriptions are available in Supplementary Materials [49–60]. Please refer to Chen et al. for more detailed information of the model [49].

2.2. Model Configurations

The model domain consists of unstructured triangular grids, comprising 114,211 elements and 60,441 nodes. The size of the element cells is variable, from about 100 m in the bay to 30 km at the open boundary of model (Figure 1e). The vertical direction is divided into seventeen sigma layers evenly. The numerical model used a cold start and was simulated from 1 December 2012 to 31 March 2013, as the observation data used for validation were collected in that year. The first three months were dedicated to model stabilization, while the last month was utilized for analysis. The model considered the effects of three runoff streams, namely the CR, the QTR, and the CER (Figure 1b). Within the study domain, the CR and QTR contribute to over 80% of the river discharge (datasets are available in <http://www.mwr.gov.cn/sj/tjgb/zghlnsgb/>, accessed on 1 January 2023) [61]. According to the field data, the annual-averaged discharge and sediment load of QR is $19.8 \times 10^9 \text{ m}^3$ and $2.5 \times 10^6 \text{ t}$, respectively. In contrast, it is $896.4 \times 10^9 \text{ m}^3$ in discharge and $389.8 \times 10^6 \text{ t}$ in sediment load in CR [62]. It was forced with various inputs, including river discharges, tides, winds, and salinity. Tides are the dominant forcing in the bay [63]. The model was compelled with different tides and salinity using the TPXO7.2 and HYCOM (HYbrid Coordinate Ocean Model). Various tides consisted of two long-period components (MF, MM), three shallow-water components (M4, MS4, MN4), four diurnal components (K1, O1, P1, Q1), and four semidiurnal components (M2, S2, N2, K2) [64]. To expedite model stabilization, the salinity initial field was based on HYCOM. Wind data were sourced from the NCEP (National Centers for Environmental Prediction). The time step of external mode was 5 s. And the time step of internal mode was 0.5 s. Table 1 presents the key parameters of the model. Only cohesive suspended sediments were taken into consideration, because they comprised the predominant portion of suspended sediment and were generally distributed across the seafloor in HZB [65]. A thorough description of the sediment parameters configuration and their rationale can be found in the article by Li et al. [44].

2.3. Model Validation

Three stations (T1 to T3) routinely collected elevation data in March 2013. An additional two stations, N1 and N2, were utilized to measure velocity and SSC data during both spring and neap tides (Figure 1b). Another sixteen stations collected depth-and-monthly averaged salinity in December 2006 (Figure 1d). Measured salinity data are from Wang et al. [37]. The validation of the model was performed by comparing the simulated and observed tidal elevation (Figure S1I), tidal currents (Figure S1II), and SSC (Figure S1III) at the field stations. To assess the performance of model, two parameters were computed to measure the discrepancies between the observation data and the model results. The correlation coefficients (CCs) and the Willmott skill score (WSS) were provided as follows [66]:

$$CC = \frac{1}{N} \sum_{i=1}^N \frac{(\eta_{mod} - \overline{\eta_{mod}})(\eta_{obs} - \overline{\eta_{obs}})}{\sigma_{mod}\sigma_{obs}} \tag{1}$$

$$WSS = 1 - \frac{\sum_{i=1}^N (\eta_{mod} - \eta_{obs})^2}{\sum_{i=1}^N (|\eta_{mod} - \overline{\eta_{obs}}| + |\eta_{obs} - \overline{\eta_{obs}}|)^2} \tag{2}$$

where η_{mod} represents the simulation results, and η_{obs} refers to the observation results. σ_{mod} and σ_{obs} are the standard deviations of the calculated and observed values, respectively. The closer the absolute values of the CCs and WSSs are to 1, the better the results of the simulation. The performance levels of WSS were categorized as: >0.2, some credibility; >0.5, high credibility [67].

Table 1. Main model parameters.

Parameters	Values
Model time steps	5 s for the outer mode, 0.5 s for the internal mode
Bottom friction coefficient	Sediment-laden BBL
Horizontal diffusion	Smagorinsky scheme
Vertical eddy viscosity	M-Y 2.5 turbulent closure
Node, element, vertical layers	114,211 elements and 60,441 nodes (reference experiment); 16 vertical layers
Open boundary condition	Sea-surface elevation time series from TPXO 7.2
Salinity initial field	Salinity time series from HYCOM
Wind	Salinity time series from HYCOM Wind time series from NCEP

The model results for water levels showed excellent agreement with the field data (Figure S1I). The CCs of the C2 and C3 stations were significantly higher than 0.97, and the WSSs were no less than 0.97 (Table S1). However, the C1 station, being at the top of HZB and affected by the tidal bore, had lower CC and WSS values, specifically 0.761 and 0.841, respectively. Regarding the current velocities at V1 and V2 stations, the model verification results were satisfactory (Figure S1II). During both spring and neap tides, the CCs and WSSs for current speed, as well as the CCs and WSSs for current direction, exceeded 0.87, 0.91, 0.88, and 0.95, respectively (Table S1). Furthermore, the verification results of SSC at each layer of the V1 and V2 stations accurately reflected the temporal trends and effectively reproduced the vertical SSC characteristics (Figure S1III). The average CCs for spring and neap tides of SSC were 0.687 and 0.499, respectively, with corresponding WSSs of 0.695 and 0.505 (Table S1). The simulated salinity of the model was in high agreement with the observed salinity, with errors not exceeding 2 psu (Table 2).

Table 2. Error analysis between modeled and observed salinity. The observed salinity data were from Wang et al. [37].

Number	Longitude/°	Latitude/°	Difference/psu
1	121.76	30.02	−1.95
2	121.81	30.12	−0.62
3	121.9	30.16	0.10
4	121.84	30.31	−1.33
5	121.77	30.25	−1.85
6	121.67	30.16	−0.57
7	121.56	30.26	−1.45
8	121.68	30.22	1.31
9	121.66	30.41	0.31
10	121.46	30.36	1.19
11	121.47	30.5	0.17
12	121.84	30.53	−0.68
13	121.66	30.61	−1.04
14	121.48	30.69	−1.63
15	121.3	30.59	1.05
16	121.29	30.48	0.46

3. Results

This section is divided by subheadings. It should provide a concise and precise description of the experimental results, their interpretation, as well as the experimental conclusions that can be drawn.

3.1. Variations in High SSC Water Bodies

During spring tides, water bodies with a bottom SSC greater than 6 kg/m³ were defined as high SSC water bodies (Figure 2). During neap tides, water bodies with a bottom SSC greater than 3 kg/m³ were defined as high SSC water bodies.

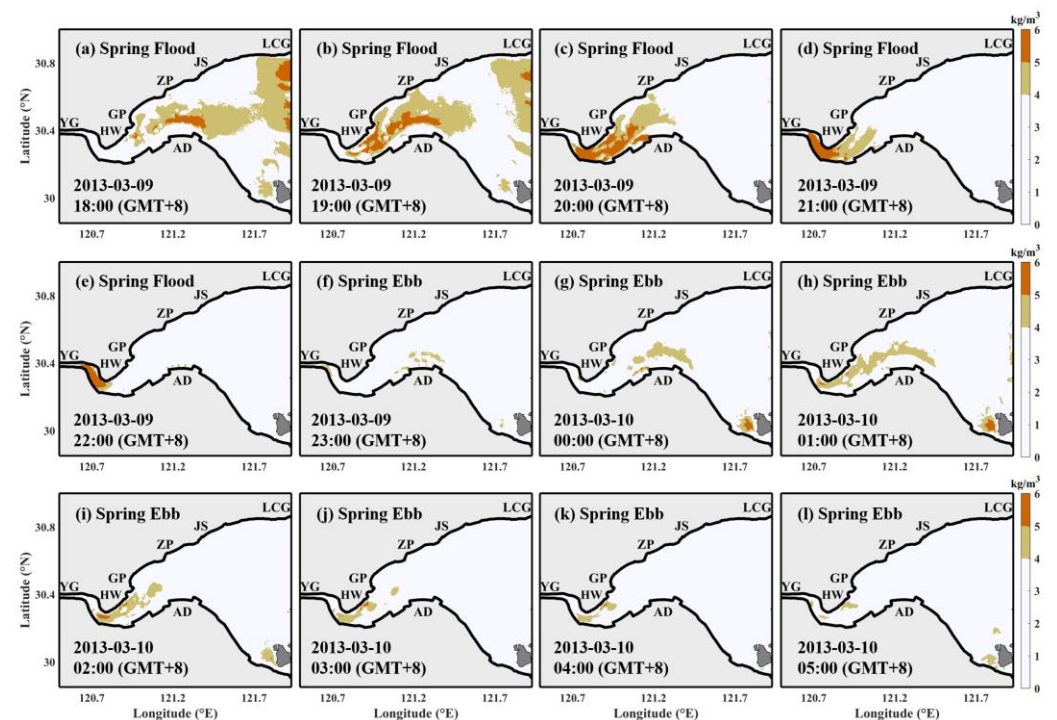


Figure 2. Spatial and temporal variations of high SSC water bodies in HZB during spring tides: (a–e) spring flood; (f–l) spring ebb.

At the onset of the spring flood, high SSC water bodies were primarily distributed from LCG to GP (Figure 2a). As the tide continued to advance (Figure 2b–e), these high SSC water bodies gradually moved landward, causing their area to shrink (Figure 2d,e). The area of high SSC water bodies fluctuated during the spring ebb, and the high SSC water bodies mainly distributed from YG to JS (Figure 2f–l). Due to the higher flow velocity during the spring flood (Figure A1a,e) in the bay compared with that during spring ebb (Figure A1c,g), the area of high SSC water bodies during the spring ebb was much smaller than that during the spring flood.

Compared with spring tides (Figure A1), the difference in flow velocity during neap tides was smaller (Figure A2). During neap tides, high SSC water bodies tended to stay between YG and ZP (Figure 3). There was a sand bar underwater. The area of the high SSC water bodies was relatively small during neap tides. In comparison to spring tides (Figure 2), the changes in the location and area of high SSC water bodies were also small during neap tides (Figure 3).

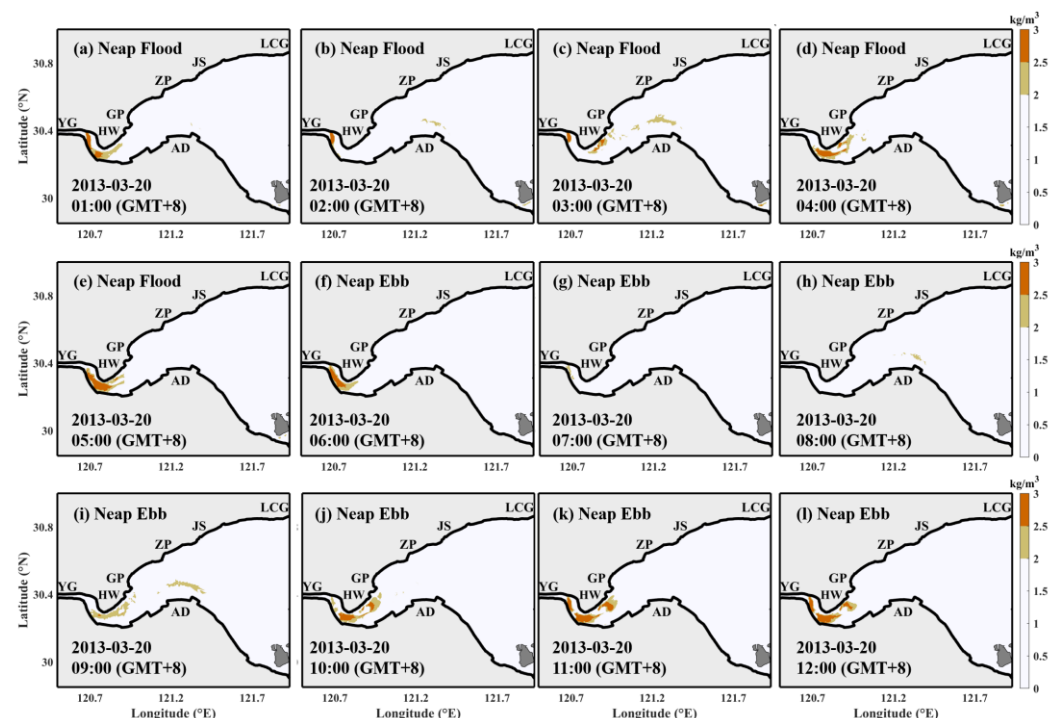


Figure 3. Spatial and temporal variations of high SSC water bodies in HZB during neap tides: (a–e) neap flood; (f–l) neap ebb.

3.2. Distribution of the TMZ

Various methods were employed to study the TMZ, including field investigations, numerical modeling, and remote sensing. Among these methods, the most commonly used approach involved setting thresholds for water quality parameters, such as sediment content, to delineate the extent of the maximum-turbidity zone within the estuary [3]. The threshold value of the TMZ could vary in different regions.

Currently, the threshold value of the TMZ in HZB has not been definitively determined. In a previous study conducted by Ye et al. [68], the threshold value of 0.7 kg/m^3 was utilized as the criterion for identifying the surface high-turbidity zone in HZB. Figure 4 displays the distribution of the TMZ in HZB for different threshold values of SSC. As the threshold value of SSC of the TMZ increased, e.g., from 0.7 kg/m^3 to 1.2 kg/m^3 , the area covered by the TMZ in HZB gradually decreased.

Under different threshold values, the TMZ in HZB was mainly distributed from YG to ZP. Combined with the distribution of high SSC water bodies during spring (Figure 2) and neap tides (Figure 3), it could be seen that the TMZ in HZB was mainly distributed

from YG to ZP. With the occurrence of ebb and flood tides, the location of the TMZ may move toward the head or the mouth of the bay, and the area of the TMZ may also be changed accordingly.

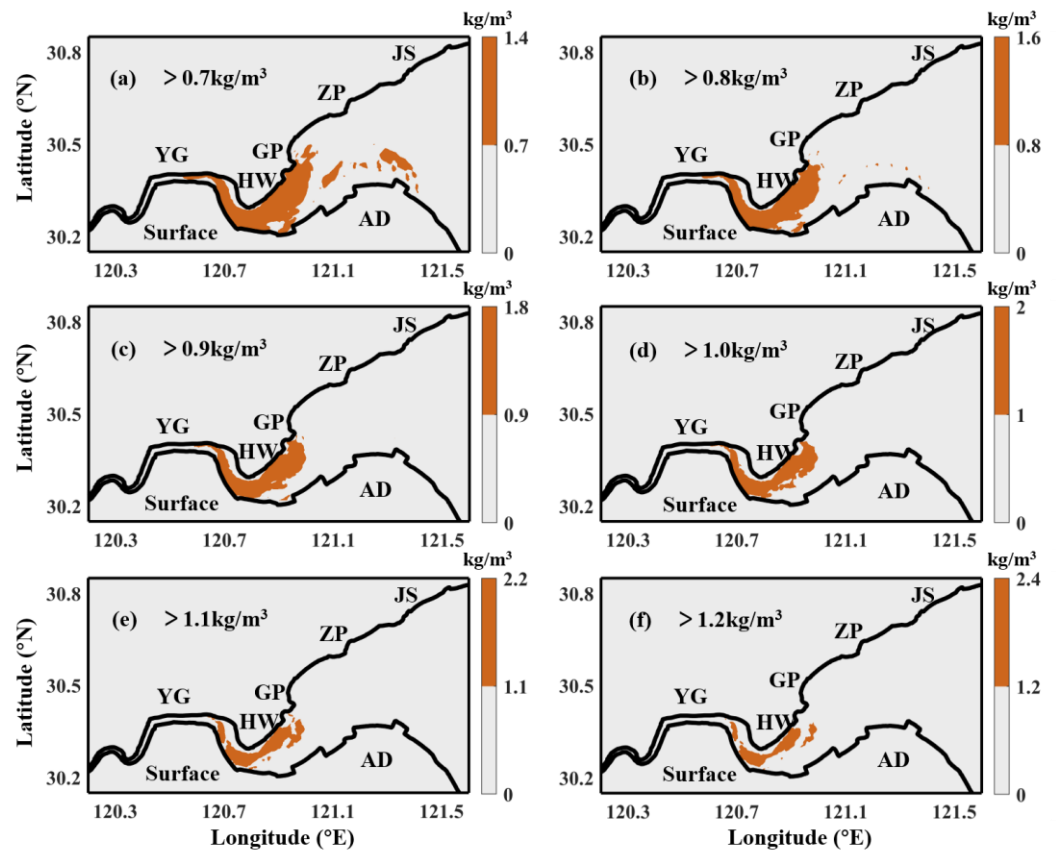


Figure 4. Variation of the surface TMZ in HZB under different threshold values. It was analyzed based on the values of the monthly mean SSC in the surface layer. The threshold values for figures (a–f) are 0.7 kg/m³ to 1.2 kg/m³, respectively.

3.3. Suspended Sediment Fluxes in the TMZ

Two cross-sections, S1 and S2, located in the TMZ, were selected to analyze the sediment fluxes in the high-turbidity zone (Figure 1c). The cross-section S1 was located near the head of HZB, and the water depth gradually increased from the northern to the southern bank. The sediment fluxes at the cross-section S1 during neap and spring tides are shown in Figure 5. Additionally, the associated residual currents are presented in Figure 6.

During spring tides (Figure 5a,d), the magnitude of suspended sediment flux was five times higher than that during neap tides (Figure 5b,e). The along-estuarine suspended sediment fluxes (Figure 5f) were approximately four times greater than the lateral suspended sediment fluxes (Figure 5c). In the section S1, all lateral suspended sediment fluxes during spring tides were directed southward. The middle of the section (2 to 5 km from the north bank) had higher lateral suspended sediment fluxes compared with those near the both banks, reaching up to 0.2 kg/m²/s (Figure 5a). Additionally, lateral suspended sediment fluxes were greater in the surface layer than in the bottom layer at the middle of the section (Figure 5a). The along-estuarine suspended sediment fluxes were seaward on the northern bank and landward on the southern bank, with higher values observed on the northern bank than on the southern bank (Figure 5d).

During neap tides (Figure 5b,e), the lateral suspended sediment fluxes at the middle of the section were southward in the surface layer and northward in the bottom layer (Figure 5b). The spatial variations in the along-estuarine suspended sediment fluxes during neap tides (Figure 5e) were similar to those during spring tides but with smaller magnitudes (Figure 5d).

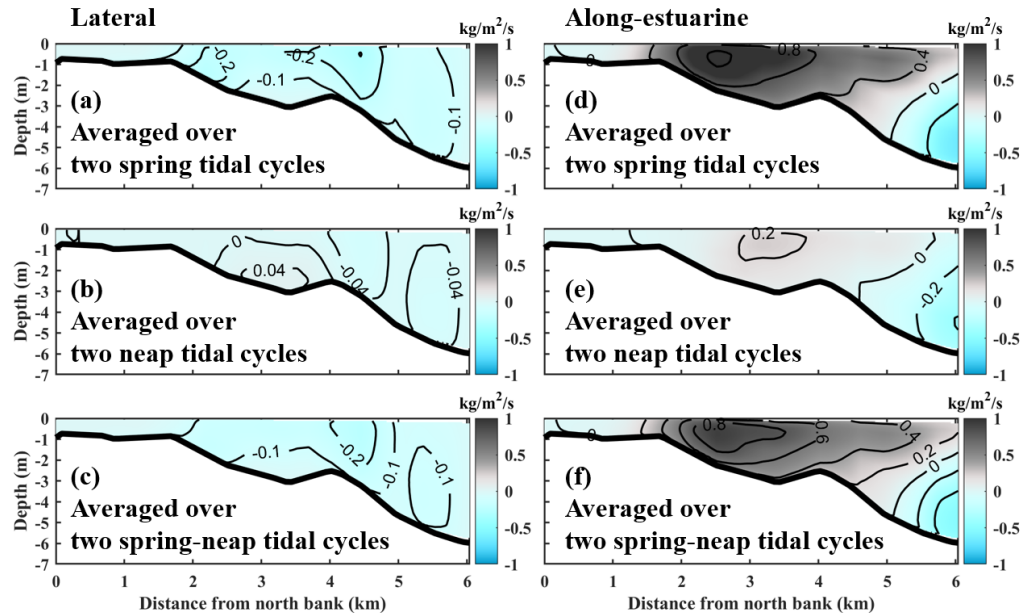


Figure 5. The distribution of suspended sediment fluxes at the cross-section S1: (a,d) present the lateral and along-estuary residual suspended sediment fluxes averaged over two spring tidal cycles; (b,e) are the same as (a,b), but for two neap tidal cycles; (c,f) are the same as (a,b), but for two spring-neap cycles. Positive values indicate seaward and northward directions.

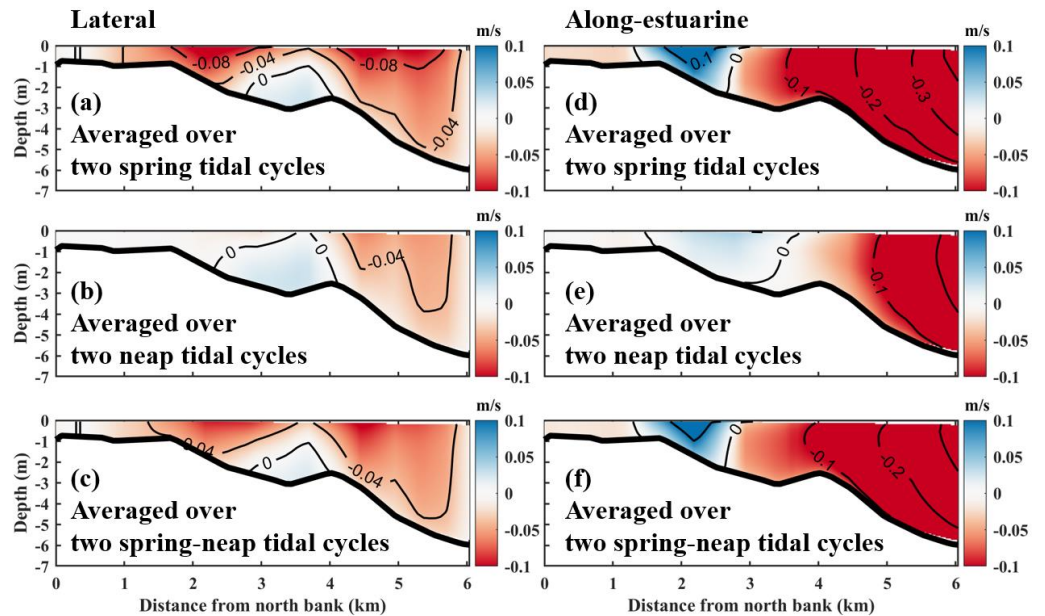


Figure 6. The distribution of residual currents at the cross-section S1: (a,d) present the lateral and along-estuary lateral residual currents averaged over two spring tidal cycles; (b,e) are the same as (a,b), but for two neap tidal cycles; (c,f) are the same as (a,b), but for two spring-neap cycles. Positive values indicate seaward and northward directions.

The suspended sediment fluxes were influenced by both lateral and along-estuarine residual currents (Figure 6), in combination with the distribution of SSC. At the middle of the section, there was a lateral residual current pattern characterized by northward bottom flow and southward surface flow (Figure 6a–c). The lateral residual currents in the surface layer were stronger than those in the bottom layer. Additionally, the along-estuary residual currents had higher magnitudes compared to the lateral residual currents (Figure 6).

The SSC was considerably higher near the bottom layer. The interaction between these residual currents and the spatial variation of SSC played a crucial role in governing the patterns of suspended sediment fluxes in the section.

The cross-section S2 was characterized by a sand bar in the middle of the section and a deep channel (15 m) near the northern bank. The sediment fluxes at the cross-section S2 during neap and spring tides are displayed in Figure 7, and the associated residual currents at the cross-section S2 are presented in Figure 8.

The along-estuarine and the lateral suspended sediment fluxes had the same order of magnitudes (Figure 7). The suspended sediment fluxes in the deep channel on the northern bank were directed northward and seaward, respectively. On the southern and northern banks, the along-estuary and the lateral suspended sediment fluxes were in opposite directions. During spring tides (Figure 7a,d), the spatial variations in suspended sediment fluxes were similar to those during neap tides (Figure 7b,e), but the magnitude of suspended sediment flux was seven times higher during spring tides than during neap tides.

The direction of the lateral residual currents at the middle of the section was southward, while the opposite directions were near the northern and southern banks (Figure 8a–c). The predominant direction of the along-estuarine residual currents was seaward (Figure 8d,e). The SSC at the section S2 exhibited a large difference in surface and bottom levels, and in spring tides and neap tides (Figure 9a–c). The interaction between residual currents and the spatial variability of the SSC also played a crucial role in the pattern of suspended sediment fluxes at this section.

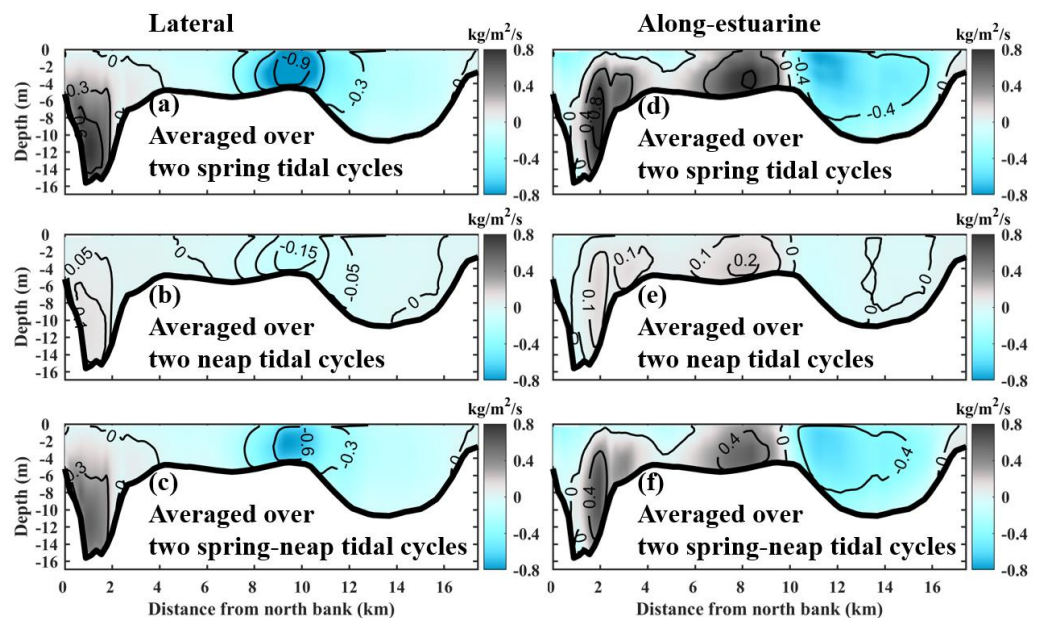


Figure 7. The distribution of suspended sediment fluxes at the cross-section S2: (a,d) present the lateral and along-estuarine residual suspended sediment fluxes averaged over two spring tidal cycles; (b,e) are the same as (a,b), but for two neap tidal cycles; (c,f) are the same as (a,b), but for two spring-neap cycles. Positive values indicate seaward and northward directions.

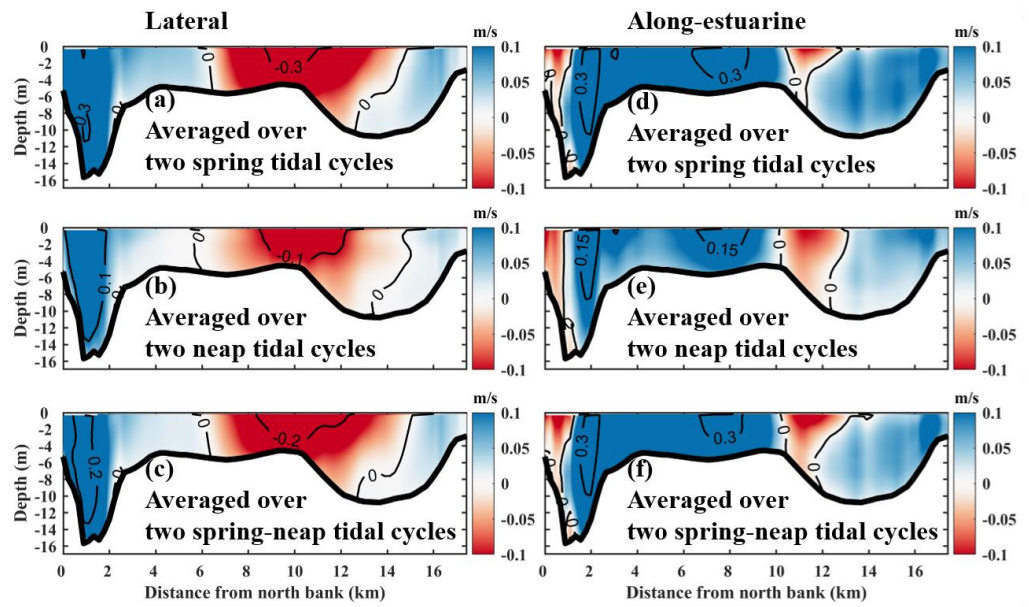


Figure 8. The distribution of residual currents at the cross-section S2: (a,d) present the lateral and along-estuarine lateral residual currents averaged over two spring tidal cycles; (b,e) are the same as (a,b), but for two neap tidal cycles; (c,f) are the same as (a,b), but for two spring-neap cycles. Positive values indicate seaward and northward directions.

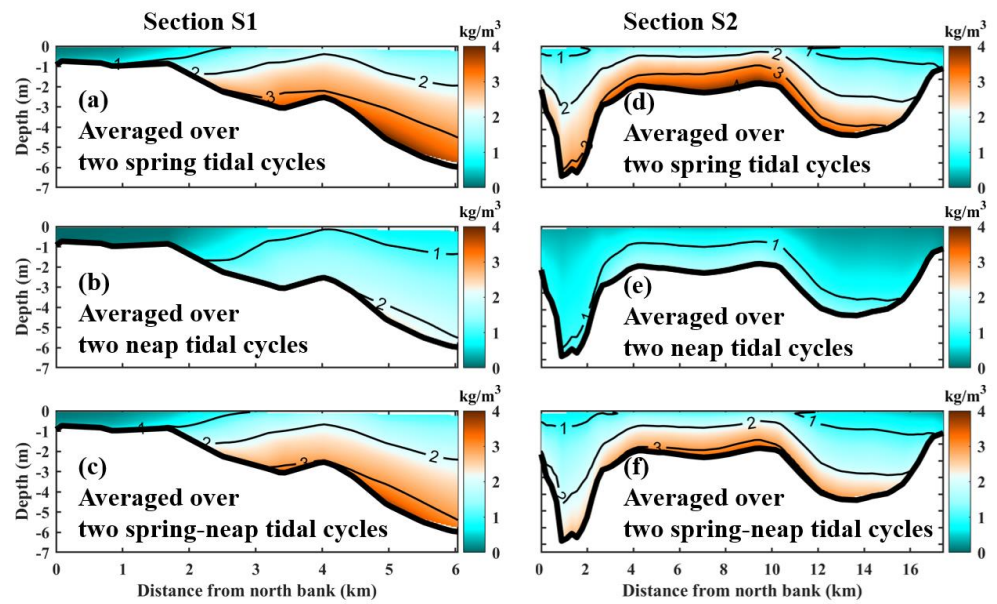


Figure 9. The distribution of SSC at the cross-section S1 and S2: (a,d) present the SSC averaged over two spring tidal cycles; (b,e) are the same as (a,b), but for two neap tidal cycles; (c,f) are the same as (a,b), but for two spring-neap cycles. Positive values indicate seaward and northward directions.

4. Discussions

4.1. Possible Causes of the Surface TMZ

The along-estuarine variation of monthly averaged current-induced shear stress in HZB is shown in Figure 10a. In general, the bed current shear stress in HZB exhibited a trend of increasing and then decreasing along the estuary. Moreover, the current-induced bed shear stress in the TMZ was larger than that in the upstream and downstream areas. The along-estuarine variation of monthly averaged surface density in HZB is shown in Figure 10b. The monthly averaged surface density showed a decreasing and then increasing

trend along the estuary. Additionally, the monthly averaged surface density in the TMZ was smaller than that in both the upstream and downstream areas.

The monthly averaged surface residual currents in HZB are shown in Figure 6a,b. The monthly averaged surface residual currents in part of the region where the TMZ was located exhibit a planar vorticity in a clockwise direction (Figure 11b). The monthly averaged surface-suspended-sediment fluxes in HZB are shown in Figure 11c,d. Generally, the region where the TMZ was located has upstream net sediment transport within a month. The direction of the monthly averaged surface-suspended-sediment fluxes in the TMZ region exhibited a clockwise vorticity and negative divergence (Figure 11d), which results in a tendency for suspended sediment to be retained and enriched within the TMZ. The divergence of monthly averaged surface-suspended-sediment fluxes in HZB is shown in Figure 10c. Positive and negative divergence alternated within the TMZ. The magnitude of monthly averaged surface-suspended-sediment fluxes (Figure 11c) and the divergence (Figure 10c) in the TMZ was larger than that in both the upstream and downstream areas.

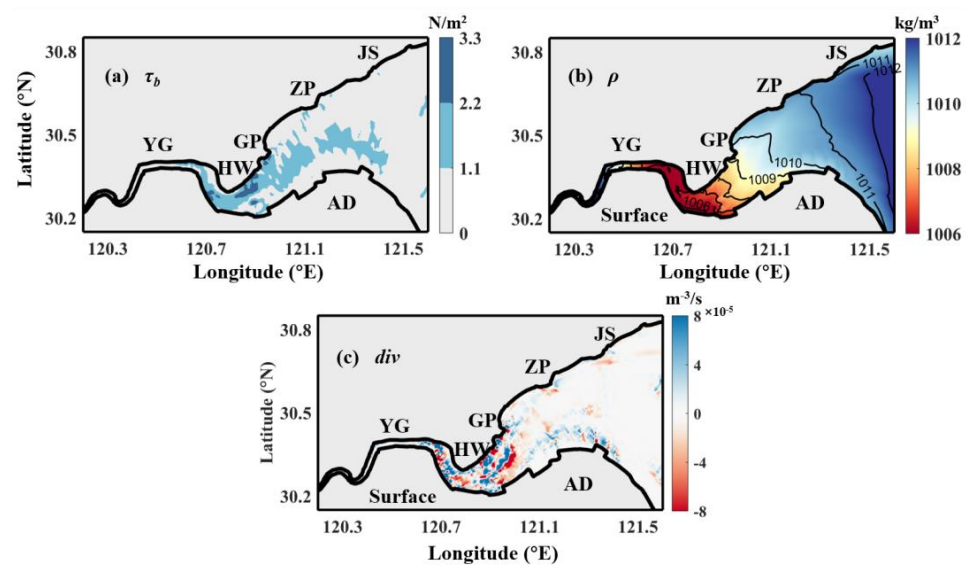


Figure 10. The variation of monthly averaged current-induced shear stress (a), surface density (b), and divergence of monthly averaged surface-suspended-sediment fluxes (c) in HZB.

4.2. Mechanisms of Sediment Fluxes in the TMZ

Suspended sediment flux is the amount of suspended sediment flowing over a given area per unit time, also known as the suspended sediment transport rates in hydrological surveys [69]. The mechanism of suspended sediment flux decomposition involves breaking down the suspended sediment flux into multiple dynamic terms, allowing for the calculation and analysis of each term. This approach helps to explore the degree of influence that different dynamic factors have on suspended sediment transport [70]. We utilized the suspended sediment flux mechanism decomposition method proposed by Dyer [71], which has been successfully applied in several estuaries worldwide [20,71]. Descriptions of the suspended sediment flux mechanism decomposition method are available in supplementary materials.

The suspended sediment fluxes averaged over two spring-neap tidal cycles at two cross-sections were decomposed by the mechanism. The results are shown in Figure 12. The Eulerian residual current represents the average of flow velocity, which illustrates the uneven distribution of flow magnitude throughout the tidal cycle. On the other hand, the Stokes residual current indicates the non-uniformity of water transport during the tidal cycle. When combined ($T_1 + T_2$), the Eulerian transport term and the Stokes transport term form the advective transport term, accounting for transport caused by the Lagrange residual flow [72]. The fluctuations in SSC over the tidal cycle are influenced, on one hand,

by advective sediment transport, and on the other hand, they are primarily driven by the tidal pumping effect ($T_3 + T_4 + T_5$).

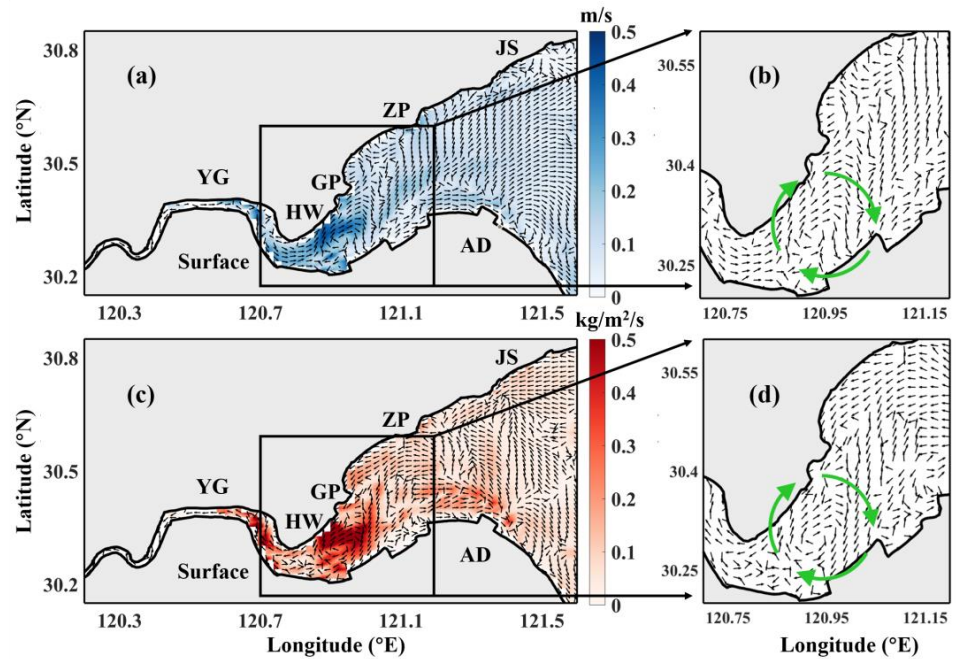


Figure 11. The distribution of monthly averaged surface residual currents (a,b) and surface-suspended-sediment fluxes (c,d) in the TMZ in HZB. Arrows only indicate direction.

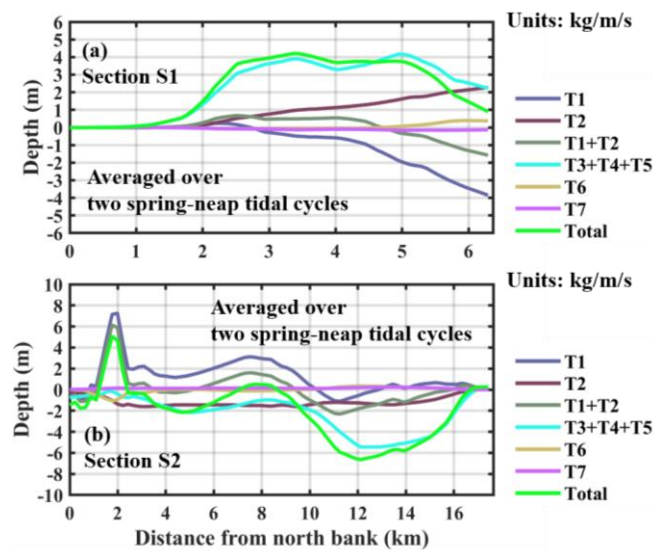


Figure 12. The mechanism controlling the suspended sediment fluxes at the section (a) S1 and (b) S2. Positive values indicate seaward. T_1 Eulerian velocity; T_2 Stokes drift; T_3 , T_4 , and T_5 tidal pumping; T_6 gravitation circulation; and T_7 changing forms of the vertical profiles of velocity and SSC in the tide.

At the section S1, the magnitudes of Eulerian transport and Stokes transport were substantial when compared with tidal pumping transport (Figure 12a). Specifically, on the southern bank, Eulerian transport could reach up to 6 kg/m/s, while Stokes transport could reach up to 4 kg/m/s. However, Eulerian transport and Stokes transport exhibited opposite directions within the main part of the section S1. As a result, the overall value of advective transport at section S1 remained relatively modest. The principal mechanism driving sediment transport at section S1 was tidal pumping.

The southern and northern banks of section S2 had different sediment transport characteristics (Figure 12b). On the northern bank, both water depths and flow velocities were large. In the deep channel, the Eulerian transport attained its maximum, reaching a magnitude of up to 7 kg/m/s, while the tidal pumping transport was negligible. Despite the Stokes transport opposed the direction of Eulerian transport, its magnitude was smaller than that of Eulerian transport. Consequently, the advective transport was still large. Within the deep channel of the northern bank, advective transport was the principal mechanism governing sediment transportation. In contrast to the northern bank, the southern bank had relatively lower water depths and smaller flow velocities. This led to reduced magnitudes of both Eulerian transport and Stokes transport, whereas tidal pumping transport had a more pronounced magnitude. Therefore, tidal pumping was the dominant mechanism governing sediment transport on the southern bank.

The along-estuary net suspended sediment fluxes and suspended sediment transport due to different mechanisms at two cross-sections in two spring-neap tidal cycles are listed in Table 3. The along-estuary net suspended sediment fluxes at the two cross-sections were in opposite directions. Specifically, the net suspended sediment flux at the section S1 was seaward, while at the section S2, it was landward. This led to easier sediment retention and deposition between the section S1 and section S2, which promoted the development of TMZ.

Table 3. The along-estuary suspended sediment fluxes at the two cross-sections in two spring-neap tidal cycles. Positive values indicate seaward suspended sediment fluxes.

Component	Section S1	Section S2
T_1 (kg/s)	−27,272	163,702
T_2 (kg/s)	23,287	−145,962
T_3 (kg/s)	−1708	−542
T_4 (kg/s)	35,458	−255,646
T_5 (kg/s)	18,867	−65,547
T_6 (kg/s)	1818	−7194
T_7 (kg/s)	−2047	18,801
Seaward (kg/s)	79,430	182,503
Landward (kg/s)	−31,027	−474,891
$T_1 + T_2$: Advection (kg/s)	−3985	17,740
$T_3 + T_4 + T_5$: Tidal pumping (kg/s)	52,617	−321,735
Total: Along-estuary net suspended sediment fluxes (kg/s)	48,403	−292,388
Advection ratio: $(T_1 + T_2)/(T_3 + T_4 + T_5)$	0.08	0.06

The suspended sediment transport at two cross-sections was primarily governed by Eulerian transport, Stokes transport, and tidal pumping transport. There were also minor contributions from gravitational circulation and the varying shapes of vertical velocity and SSC profiles within the tidal cycle. Eulerian transport and Stokes transport exhibited comparable magnitudes but opposite directions at both cross-sections. Moreover, sediment transport resulting from tidal pumping largely outweighed advective sediment transport at both sections, with their directions opposing each other. The advection ratios for Sections 1 and 2 were 0.08 and 0.06, respectively, signifying that tidal pumping assumes a more substantial role in suspended sediment transport along the estuary in HZB (Table 3).

Suspended sediment transport caused by Eulerian transport at section S1 was landward, whereas at section S2, it moved seaward. In the case of Stokes transport, suspended sediment transport at both sections S1 and S2 was seaward, while at section S2, it was landward. Additionally, suspended sediment transport induced by tidal pumping at section S1 was seaward, but at section S2, it moved landward.

5. Conclusions

A three-dimensional baroclinic numerical model has been established utilizing the FVCOM and fully validated using the field data. The model has adeptly replicated the hydro-sediment dynamics in macro-tidal turbid HZB that considers salinity, high turbidity, sediment flocculation, and water-sediment density coupling. The distribution of the TMZ in HZB is analyzed and discussed. The main conclusions are as follows.

(1) The locations and areas of high SSC water bodies change with the flood and ebb tides during spring and neap tides. At different thresholds, the area of TMZ varies. However, they are predominantly situated from YG to ZP.

(2) Along the estuary, there is an ascending-to-descending trend observed in the monthly averaged bed current shear stress, while the monthly averaged density displays a reverse pattern. The direction of the monthly averaged surface-suspended-sediment fluxes, where the TMZ is situated, displayed a clockwise circular pattern. The along-estuary net suspended sediment flux at section S1 is seaward, while at section S2, it is landward. All these dynamic characteristics collectively facilitates the retention, deposition, and enrichment of sediment within the TMZ.

(3) The interaction between the residual currents and the spatial variation of SSC plays a crucial role in governing the patterns of suspended sediment fluxes in the two sections. The suspended sediment flux at two specific cross-sections is primarily influenced by Eulerian transport, Stokes transport, and tidal pumping transport. At cross-section S1, the primary mechanism driving sediment transport is tidal pumping. At cross-section S2, situated within the deep channel of the north bank, advective transport is the principal governing mechanism for sediment transportation. However, on the south bank of cross-section S2, tidal pumping remains the dominant mechanism governing sediment transport.

The above conclusions provide data for the future study in estuarine geomorphology. More data are needed to strength the conclusions in future studies.

Supplementary Materials: The following supporting information can be downloaded at: <https://www.mdpi.com/article/10.3390/jmse11102004/s1>.

Author Contributions: Conceptualization, X.C. and L.L.; data curation, X.C.; formal analysis, X.C.; funding acquisition, H.S., J.Y. and L.L.; investigation, X.C.; project administration, H.S. and L.L.; supervision, L.L.; validation, X.C. and L.L.; visualization, X.C.; writing—original draft, X.C.; writing—review and editing, X.C. and L.L. All authors have read and agreed to the published version of the manuscript.

Funding: This research was funded by the Key R&D Program of Guangxi (Guike AB22080081), and the Science Technology Department of Zhejiang Province of China (2021C03180, 2022C03044). Data and samples were partially collected onboard of R/V “Zheyuke2”/“Runjiang1” implementing the open research cruise NORC2021-03 supported by NSFC Shiptime Sharing Project (project number: 42049903).

Institutional Review Board Statement: Not applicable.

Informed Consent Statement: Not applicable.

Data Availability Statement: Not applicable.

Acknowledgments: We are grateful for H.Q. for providing salinity data.

Conflicts of Interest: The authors declare no conflict of interest.

Appendix A

Table A1. Acronyms defined.

Acronyms	Full Name
HZB	Hangzhou Bay
TMZ	Turbidity maximum zone

Table A1. Cont.

Acronyms	Full Name
SSC	Suspended sediment concentration
CR	The Changjiang River
QTR	The Qiantangjiang River
CER	The Cao'e'jiang River
YG	Yanguan (toponymy in HZB)
HW	Huangwan (toponymy in HZB)
GP	Ganpu (toponymy in HZB)
ZP	Zhapu (toponymy in HZB)
JS	Jinshan (toponymy in HZB)
LCG	Luchaogang (toponymy in HZB)
AD	Andong shoal (toponymy)
SX	Shaoxing (toponymy in HZB)
ZH	Zhenhai (toponymy in HZB)
WJY	Wenjiayan (toponymy)

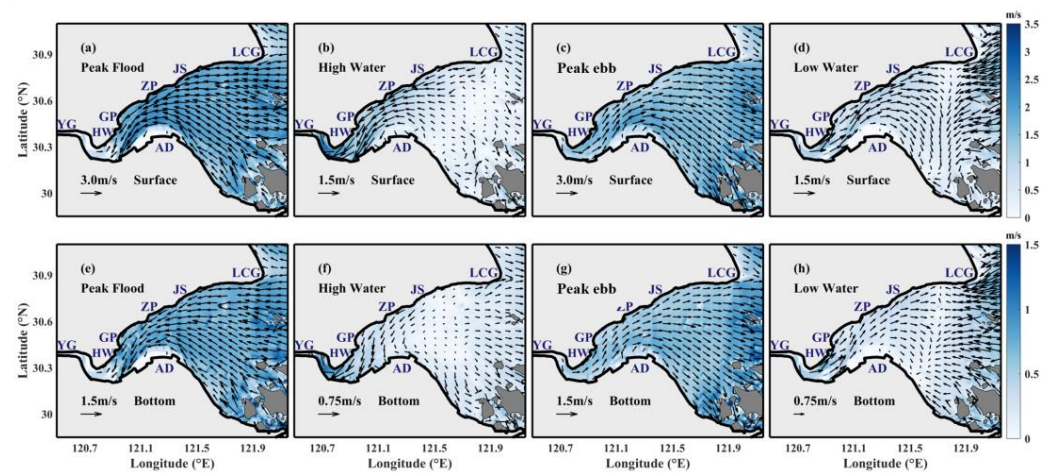


Figure A1. Flow velocities during spring tides: (a) peak flood, (b) high water, (c) peak ebb, (d) low water; (e–h) are the same as (a,b) except for bottom velocities.

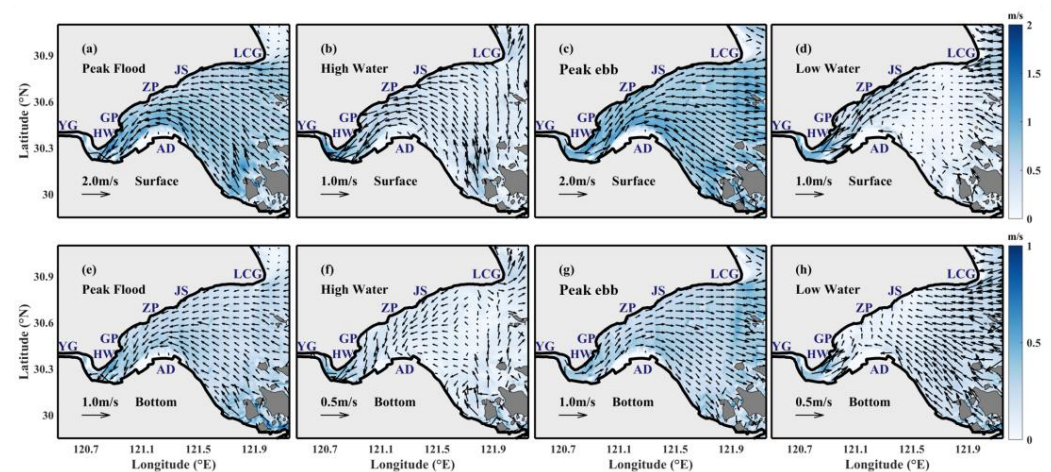


Figure A2. Flow velocities during neap tides: (a) peak flood, (b) high water, (c) peak ebb, (d) low water; (e–h) are the same as (a,b) except for bottom velocities.

References

1. Vinh, V.D.; Tu, T.A.; Lan, T.D.; Tien, N.N. Characteristics of suspended particulate matter and the coastal turbidity maximum areas of the Mekong River. *J. Environ. Sci. Eng. A* **2015**, *4*, 67–78.
2. Shi, Z.; Xu, J.; Huang, X.; Zhang, X.; Jiang, Z.; Ye, F.; Liang, X. Relationship between nutrients and plankton biomass in the turbidity maximum zone of the Pearl River Estuary. *J. Environ. Sci.* **2017**, *57*, 72–84. [[CrossRef](#)] [[PubMed](#)]
3. Wang, C.; Zhou, C.; Chen, S.; Xie, Y.; Li, D.; Yang, J.; Zhou, X.; Li, Y.; Wang, D.; Liu, Y. Retrospect and perspective of the estuarine turbidity maximum zone researches. *Kexue Tongbao/Chin. Sci. Bull.* **2021**, *66*, 2328–2342. [[CrossRef](#)]
4. Burchard, H.; Schuttelaars, H.M.; Ralston, D.K. Sediment trapping in estuaries. *Annu. Rev. Mar. Sci.* **2018**, *10*, 371–395. [[CrossRef](#)] [[PubMed](#)]
5. Xiao, Y.; Wu, Z.; Cai, H.; Tang, H. Suspended sediment dynamics in a well-mixed estuary: The role of high suspended sediment concentration (SSC) from the adjacent sea area. *Estuar. Coast. Shelf Sci.* **2018**, *209*, 191–204. [[CrossRef](#)]
6. Yang, Y.; Li, Y.; Sun, Z.; Fan, Y. Suspended sediment load in the turbidity maximum zone at the Yangtze River Estuary: The trends and causes. *J. Geogr. Sci.* **2014**, *24*, 129–142. [[CrossRef](#)]
7. Ji, R.; Lu, Y.; Zhan, X. Study on the morphodynamic evolution processes in the Maozhou Estuary of the Lingding Bay. *Adv. Water Sci.* **2019**, *30*, 781–788.
8. Hou, Q.; Lu, Y.; Wang, Z.; Mo, S. Cumulative response of estuarine bay hydrodynamic environment to human activities: Example of Lingding Bay of the Pearl River Estuary. *Adv. Water Sci.* **2019**, *30*, 789–799.
9. Zhu, L.; Xu, Q.; Zhang, O.; Yang, Y.; Wang, W. Sedimentation at estuary of 66 tributaries in the Three Gorges Reservoir. *Sci. Sin. Technol.* **2019**, *49*, 552–564. [[CrossRef](#)]
10. Jiang, X.; Lu, B.; He, Y. Response of the turbidity maximum zone to fluctuations in sediment discharge from river to estuary in the Changjiang Estuary (China). *Estuar. Coast. Shelf Sci.* **2013**, *131*, 24–30. [[CrossRef](#)]
11. Jalón-Rojas, I.; Schmidt, S.; Sottolichio, A.; Bertier, C. Tracking the turbidity maximum zone in the Loire Estuary (France) based on a long-term, high-resolution and high-frequency monitoring network. *Cont. Shelf Res.* **2016**, *117*, 1–11. [[CrossRef](#)]
12. Zhang, X.; Chen, X.; Dou, X.; Zhao, X.; Xia, W.; Jiao, J.; Xu, H. Study on formation mechanism of turbidity maximum zone and numerical simulations in the macro tidal estuaries. *Adv. Water Sci.* **2019**, *30*, 84–92.
13. Lee, D.Y.; Keller, D.P.; Crump, B.C.; Hood, R.R. Community metabolism and energy transfer in the Chesapeake Bay estuarine turbidity maximum. *Mar. Ecol. Prog. Ser.* **2012**, *449*, 65–82. [[CrossRef](#)]
14. Dyer, K.; Bale, A.; Christie, M.; Feates, N.; Jones, S.; Manning, A. The turbidity maximum in a mesotidal estuary, the Tamar estuary, UK: II. The floc properties. In *Proceedings in Marine Science*; Elsevier: Amsterdam, The Netherlands, 2002; Volume 5, pp. 219–232.
15. Doxaran, D.; Froidefond, J.-M.; Castaing, P.; Babin, M. Dynamics of the turbidity maximum zone in a macrotidal estuary (the Gironde, France): Observations from field and MODIS satellite data. *Estuar. Coast. Shelf Sci.* **2009**, *81*, 321–332. [[CrossRef](#)]
16. Azhikodan, G.; Yokoyama, K. Seasonal morphodynamic evolution in a meandering channel of a macrotidal estuary. *Sci. Total Environ.* **2019**, *684*, 281–295. [[CrossRef](#)] [[PubMed](#)]
17. Yu, Y.; Zhang, H.; Lemckert, C. Salinity and turbidity distributions in the Brisbane River estuary, Australia. *J. Hydrol.* **2014**, *519*, 3338–3352. [[CrossRef](#)]
18. Kitheka, J.U.; Mavuti, K.M.; Nthenge, P.; Obiero, M. The Dynamics of the Turbidity Maximum Zone in a Tropical Sabaki Estuary in Kenya. *J. Environ. Sci. Water Resour.* **2014**, *3*, 86–103.
19. Schubel, J. Turbidity maximum of the northern Chesapeake Bay. *Science* **1968**, *161*, 1013–1015. [[CrossRef](#)]
20. Wai, O.; Wang, C.; Li, Y.S.; Li, X. The formation mechanisms of turbidity maximum in the Pearl River estuary, China. *Mar. Pollut. Bull.* **2004**, *48*, 441–448. [[CrossRef](#)]
21. Althausen, J., Jr.; Kjerfve, B. Distribution of suspended sediment in a partially mixed estuary, Charleston Harbor, South Carolina, USA. *Estuar. Coast. Shelf Sci.* **1992**, *35*, 517–531. [[CrossRef](#)]
22. Jalón-Rojas, I.; Schmidt, S.; Sottolichio, A. Turbidity in the fluvial Gironde Estuary (southwest France) based on 10-year continuous monitoring: Sensitivity to hydrological conditions. *Hydrol. Earth Syst. Sci.* **2015**, *19*, 2805–2819. [[CrossRef](#)]
23. Bogen, J. The hysteresis effect of sediment transport systems. *Nor. J. Geogr.* **1980**, *34*, 45–54. [[CrossRef](#)]
24. Knaapen, M.; Kelly, D.M. Modelling sediment transport with hysteresis effects. In *Proceedings of the TELEMAC-MASCARET User Conference 2011*, Paris, France, 19–21 October 2011.
25. Shen, H.; He, S.; Pan, D.; Li, J. A study of turbidity maximum in the Changjiang estuary. *Acta Geogr. Sin.* **1992**, *47*, 472–479.
26. Kranck, K. Flocculation of suspended sediment in the sea. *Nature* **1973**, *246*, 348–350. [[CrossRef](#)]
27. Manning, A.; Langston, W.; Jonas, P. A review of sediment dynamics in the Severn Estuary: Influence of flocculation. *Mar. Pollut. Bull.* **2010**, *61*, 37–51. [[CrossRef](#)] [[PubMed](#)]
28. Chen, S.; Huang, W.; Wang, H.; Li, D. Remote sensing assessment of sediment re-suspension during Hurricane Frances in Apalachicola Bay, USA. *Remote Sens. Environ.* **2009**, *113*, 2670–2681. [[CrossRef](#)]
29. Schettini, C.A.F.; Paiva, B.P.; Batista, R.d.A.L.; Oliveira Filho, J.C.d.; Truccolo, E.C. Observation of an estuarine turbidity maximum in the highly impacted Capibaribe Estuary, Brazil. *Braz. J. Oceanogr.* **2016**, *64*, 185–190. [[CrossRef](#)]
30. Laurel-Castillo, J.; Valle-Levinson, A. Tidal and subtidal variations in water level produced by ocean-river interactions in a subtropical estuary. *J. Geophys. Res. Ocean.* **2020**, *125*, e2018JC014116. [[CrossRef](#)]
31. Wellershaus, S. Turbidity maximum and mud shoaling in the Weser estuary. *Arch. Hydrobiol.* **1981**, *92*.

32. Sun, Z.-L.; Shao, K.; Xu, D.; Liang, X. Fractional bedload transport in turbid waters. *Shuili Xuebao J. Hydraul. Eng.* **2012**, *43*, 99–105.
33. Liu, J.; Li, Y.; Pan, Q.; Zhang, T. Suspended sediment transport and turbidity maximum in a macro-tidal estuary with mountain streams: A case study of the Oujiang Estuary. *Cont. Shelf Res.* **2023**, *255*, 104924. [[CrossRef](#)]
34. Hamblin, P. Observations and model of sediment transport near the turbidity maximum of the Upper Saint Lawrence Estuary. *J. Geophys. Res. Ocean.* **1989**, *94*, 14419–14428. [[CrossRef](#)]
35. He, X.; Bai, Y.; Pan, D.; Huang, N.; Dong, X.; Chen, J.; Chen, C.-T.A.; Cui, Q. Using geostationary satellite ocean color data to map the diurnal dynamics of suspended particulate matter in coastal waters. *Remote Sens. Environ.* **2013**, *133*, 225–239. [[CrossRef](#)]
36. Lin, C.-M.; Zhuo, H.-C.; Gao, S. Sedimentary facies and evolution in the Qiantang River incised valley, eastern China. *Mar. Geol.* **2005**, *219*, 235–259. [[CrossRef](#)]
37. Wang, Y.; Chen, J.; Zhou, F.; Zhang, W.; Hao, Q. Spatial and temporal variations of chlorophyll a and primary productivity in the Hangzhou Bay. *J. Mar. Sci. Eng.* **2022**, *10*, 356. [[CrossRef](#)]
38. Pan, C.-H.; Zeng, J.; Tang, Z.-W.; Shi, Y.-B. A study of sediment characteristics and riverbed erosion/deposition in Qiantang estuary. *Hydro-Sci. Eng.* **2015**, *1*, 1–7.
39. Wu, M.; Xu, J.; Feng, Y. Spacial-temporal distribution of suspended sediment concentration in Hangzhou Bay. *J. Sediment Res.* **2011**, *1*, 33–37.
40. Dong, Y. Grain size features of bed material and sedimentary source in the Hangzhou Bay. *Shanghai Geol.* **1991**, *12*, 22–51.
41. Li, L.; Ren, Y.; Wang, X.H.; Xia, Y. Sediment dynamics on a tidal flat in macro-tidal Hangzhou Bay during Typhoon Mitag. *Cont. Shelf Res.* **2022**, *237*, 104684. [[CrossRef](#)]
42. Song, Z.; Shi, W.; Zhang, J.; Hu, H.; Zhang, F.; Xu, X. Transport mechanism of suspended sediments and migration trends of sediments in the central Hangzhou Bay. *Water* **2020**, *12*, 2189. [[CrossRef](#)]
43. Xie, D.-F.; Shu, G.; Wang, Z.-B.; Pan, C.-H. Numerical modeling of tidal currents, sediment transport and morphological evolution in Hangzhou Bay, China. *Int. J. Sediment Res.* **2013**, *28*, 316–328. [[CrossRef](#)]
44. Li, L.; Ren, Y.; Ye, T.; Wang, X.H.; Hu, J.; Xia, Y. Positive Feedback Between the Tidal Flat Variations and Sediment Dynamics: An Example Study in the Macro-Tidal Turbid Hangzhou Bay. *J. Geophys. Res. Ocean.* **2023**, *128*, e2022JC019414. [[CrossRef](#)]
45. Du, P.; Ding, P.; Hu, K. Simulation of three-dimensional cohesive sediment transport in Hangzhou Bay, China. *Acta Oceanol. Sin.* **2010**, *29*, 98–106. [[CrossRef](#)]
46. Huang, J.; Yuan, R.; Zhu, J. Numerical simulation and analysis of water and suspended sediment transport in Hangzhou Bay, China. *J. Mar. Sci. Eng.* **2022**, *10*, 1248. [[CrossRef](#)]
47. Hu, Y.; Yu, Z.; Zhou, B.; Li, Y.; Yin, S.; He, X.; Peng, X.; Shum, C. Tidal-driven variation of suspended sediment in Hangzhou Bay based on GOCI data. *Int. J. Appl. Earth Obs. Geoinf.* **2019**, *82*, 101920. [[CrossRef](#)]
48. Cai, L.; Tang, D.; Li, X.; Zheng, H.; Shao, W. Remote sensing of spatial-temporal distribution of suspended sediment and analysis of related environmental factors in Hangzhou Bay, China. *Remote Sens. Lett.* **2015**, *6*, 597–603. [[CrossRef](#)]
49. Chen, C.; Liu, H.; Beardsley, R.C. An unstructured grid, finite-volume, three-dimensional, primitive equations ocean model: Application to coastal ocean and estuaries. *J. Atmos. Ocean. Technol.* **2003**, *20*, 159–186. [[CrossRef](#)]
50. Smagorinsky, J. General circulation experiments with the primitive equations: I. The basic experiment. *Mon. Weather Rev.* **1963**, *91*, 99–164. [[CrossRef](#)]
51. Mellor, G.L.; Yamada, T. Development of a turbulence closure model for geophysical fluid problems. *Rev. Geophys.* **1982**, *20*, 851–875. [[CrossRef](#)]
52. Wu, L.; Chen, C.; Guo, P.; Shi, M.; Qi, J.; Ge, J. A FVCOM-based unstructured grid wave, current, sediment transport model, I. Model description and validation. *J. Ocean Univ. China* **2011**, *10*, 1–8. [[CrossRef](#)]
53. Warner, J.C.; Sherwood, C.R.; Signell, R.P.; Harris, C.K.; Arango, H.G. Development of a three-dimensional, regional, coupled wave, current, and sediment-transport model. *Comput. Geosci.* **2008**, *34*, 1284–1306. [[CrossRef](#)]
54. Van Prooijen, B.; Winterwerp, J. A stochastic formulation for erosion of cohesive sediments. *J. Geophys. Res. Ocean.* **2010**, *115*, C01005. [[CrossRef](#)]
55. Winterwerp, J.C. Stratification effects by cohesive and noncohesive sediment. *J. Geophys. Res. Ocean.* **2001**, *106*, 22559–22574. [[CrossRef](#)]
56. Hansen, D.V.; Rattray, M., Jr. Gravitational circulation in straits and estuaries. *J. Mar. Res.* **1966**. [[CrossRef](#)]
57. Burchard, H.; Hetland, R.D.; Schulz, E.; Schuttelaars, H.M. Drivers of residual estuarine circulation in tidally energetic estuaries: Straight and irrotational channels with parabolic cross section. *J. Phys. Oceanogr.* **2011**, *41*, 548–570. [[CrossRef](#)]
58. Wang, X.H. Tide-induced sediment resuspension and the bottom boundary layer in an idealized estuary with a muddy bed. *J. Phys. Oceanogr.* **2002**, *32*, 3113–3131. [[CrossRef](#)]
59. Wang, X.H.; Byun, D.S.; Wang, X.L.; Cho, Y.K. Modelling tidal currents in a sediment stratified idealized estuary. *Cont. Shelf Res.* **2005**, *25*, 655–665. [[CrossRef](#)]
60. Adams, C.E., Jr.; Weatherly, G.L. Some effects of suspended sediment stratification on an oceanic bottom boundary layer. *J. Geophys. Res. Ocean.* **1981**, *86*, 4161–4172. [[CrossRef](#)]
61. Wenwu, Y. Water and sediment characteristics and their scouring and silting law in the three Rivers of Ningbo. *J. Water Resour. Water Transp. Eng.* **2011**, *4*, 143–148.
62. Liu, C.; Sui, J.; He, Y.; Hirshfield, F. Changes in runoff and sediment load from major Chinese rivers to the Pacific Ocean over the period 1955–2010. *Int. J. Sediment Res.* **2013**, *28*, 486–495. [[CrossRef](#)]

63. Li, N.; Mao, Z.; Zhang, Q. The impact of physical processes on pollutant transport in Hangzhou Bay. *Chin. J. Oceanol. Limnol.* **2009**, *27*, 266–276. [[CrossRef](#)]
64. Egbert, G.D.; Erofeeva, S.Y. Efficient inverse modeling of barotropic ocean tides. *J. Atmos. Ocean. Technol.* **2002**, *19*, 183–204. [[CrossRef](#)]
65. Brenon, I.; Le Hir, P. Modelling the turbidity maximum in the Seine estuary (France): Identification of formation processes. *Estuar. Coast. Shelf Sci.* **1999**, *49*, 525–544. [[CrossRef](#)]
66. Murphy, A.H. Climatology, persistence, and their linear combination as standards of reference in skill scores. *Weather. Forecast.* **1992**, *7*, 692–698. [[CrossRef](#)]
67. Onken, R. Forecast skill score assessment of a relocatable ocean prediction system, using a simplified objective analysis method. *Ocean. Sci.* **2017**, *13*, 925–945. [[CrossRef](#)]
68. Ye, T.; Li, L.; Yao, Y.; Xia, Y.; Guan, W. Inter-Annual Variability of the Turbidity Maximum Zone in Hangzhou Bay Based on Landsat Imagery. *Geomat. Inf. Sci. Wuhan Univ.* **2019**, *44*, 1377–1384.
69. Simon, A.; Dickerson, W.; Heins, A. Suspended-sediment transport rates at the 1.5-year recurrence interval for ecoregions of the United States: Transport conditions at the bankfull and effective discharge? *Geomorphology* **2004**, *58*, 243–262. [[CrossRef](#)]
70. Sommerfield, C.K.; Wong, K.C. Mechanisms of sediment flux and turbidity maintenance in the Delaware Estuary. *J. Geophys. Res. Ocean.* **2011**, *116*, C01005. [[CrossRef](#)]
71. Dyer, K.R. *Estuaries: A Physical Introduction*; John Wiley & Sons: London, UK, 1973.
72. Song, Y.-G.; Lu, Y.-J.; Liu, X.-C. Water and sediment transport mechanism in the Huangpu River Estuary, Shanghai. *J. East China Norm. Univ. (Nat. Sci.)* **2016**, *3*, 136–145.

Disclaimer/Publisher’s Note: The statements, opinions and data contained in all publications are solely those of the individual author(s) and contributor(s) and not of MDPI and/or the editor(s). MDPI and/or the editor(s) disclaim responsibility for any injury to people or property resulting from any ideas, methods, instructions or products referred to in the content.